Dual-Sensitizer Photoanode for Bromide Oxidation

Michael D. Turlington, Matthew D. Brady and Gerald J. Meyer*

Department of Chemistry, University of North Carolina at Chapel Hill, Murray Hall 2202B,
Chapel Hill, North Carolina 27599-3290

Abstract

A dual-sensitizer mesoporous thin film photoanode has been characterized for visible light driven bromide oxidation in aqueous pH 5.6 solution. The thin film is comprised of interconnected nanoparticles with a rutile SnO_2 core, a TiO_2 shell sensitized to visible light with (1-cyano-2-(4-(di-p-tolylamino)phenyl)vinyl)phosphonic acid (**Org**), and an Al_2O_3 overlayer to which $[(bpz)_2(4,4'-(PO_3H_2)_2-2,2\text{-bipyridine}]^{2+}$ (**Ru**) was anchored, where bpz is 2,2'-bipyrazine. This material herein referred to as CS|**Org**|Al_2O_3|**Ru**, is composed of two spatially isolated sensitizers, **Org** a potent photoreductant that facilitates quantitative excited-state electron injection into the core/shell nanoparticle ($\phi = 1$), and **Ru** that regenerates **Org**^{ox} and catalyzes bromide oxidation. The **Ru**^{ox} product was found to react with bromide with a rate constant $k_{reg} = 2\times10^7\ M^{-1}\ s^{-1}$. In an operational HBr splitting cell, the dual-sensitizer photoanode sustained 200 $\mu A/cm^2$ of photocurrent, significantly outperforming photoanodes with either **Org** (40 $\mu A/cm^2$) or **Ru** (2 $\mu A/cm^2$) alone. The photocurrent enhancement was achieved in spite of a non-productive reductive quenching pathway (**Org** + **Ru*** → **Org**^{ox} + **Ru**^{red}), that was identified through transient absorption spectroscopy. The thickness of the insulating Al_2O_3 layer between the two sensitizers was found to impact the yield of the reductive quenching pathway. Time resolved anisotropy measurements with Monte-Carlo simulations provided the rate constant for lateral intermolecular **Ru* + Ru → Ru + Ru*** energy transfer across an insulating oxide surface, behavior expected to enhance the probability of encounters with **Org**^{ox} in CS|**Org**|Al_2O_3|**Ru**. The data indicate that a dual-sensitizer photoanode approach could be utilized for mediated water oxidation that exploits conditions where catalysis is more favorable.

Keywords: Dual-sensitizer, bromide oxidation, ruthenium polypyridyl, anisotropy, photocurrents, core-shell

Introduction

Water splitting provides a viable means of generating a sustainable and storable fuel from sunlight.[1–10] This "holy grail" of solar energy storage has been performed with a dye-sensitized photoelectrosynthesis cells, wherein oxidation ($2H_2O \rightarrow O_2 + 4e^-$) occurs at a dye-sensitized anodes and reduction ($2H_2O + 4e^- \rightarrow 2H_2$) at dark Pt electrodes.[11-30] In a typical cell, the photoanode is composed of a wide band gap semiconducting metal oxide sensitized to visible light by a molecular dye often called a sensitizer, S^0. Photoexcitation of S^0 results in excited-state electron injection into the semiconductor yielding an interfacial charge-separated state $TiO_2(e\text{-})|S^+$. The oxidizing equivalent is then transferred from S^+ to a catalyst via thermal electron transfer, which regenerates S^0. After four oxidizing equivalents have accumulated on the catalyst, water oxidation occurs, completing the anodic half reaction. The photoinjected electrons are transported to a platinum cathode that catalyzes proton reduction, Figure 1A. Herein are described first steps toward an alternative strategy wherein bromine is generated as a redox mediator for water oxidation through dye-sensitization, Figure 1B.

The efficiency of water splitting is generally limited by the oxidation half reaction, as the accumulation of four redox equivalents on a single catalyst occurs in kinetic competition with deleterious charge recombination reactions.[27–30] Recent literature reports have shown that unwanted back-electron transfer reactions from the semiconductor to the oxidized dye and/or catalyst can be inhibited through the use of core/shell metal oxide materials,[31] redox gradients that vectorally separate charge,[12,32] chemical linkers that position the catalyst farther from the dye-sensitized interface,[33] or a combination of these strategies.[34] However, the solar conversion efficiency still remains far from optimal. An alternative strategy is to physically separate the water oxidation catalyst from the dye-sensitized photoanode. In this design, dye-sensitization creates a mobile oxidant that is thermodynamically capable of initiating water oxidation at a remote catalytic site.[35] Efficient dye-sensitized generation of potent oxidants that serve as mediators for water oxidation is therefore crucial to the successful implementation of this strategy. Iodine generation, for example, is well known to occur nearly quantitatively in dye-sensitized solar cells, but I_2 is not a strong enough oxidant for water oxidation in neutral or acidic aqueous solutions.[36]

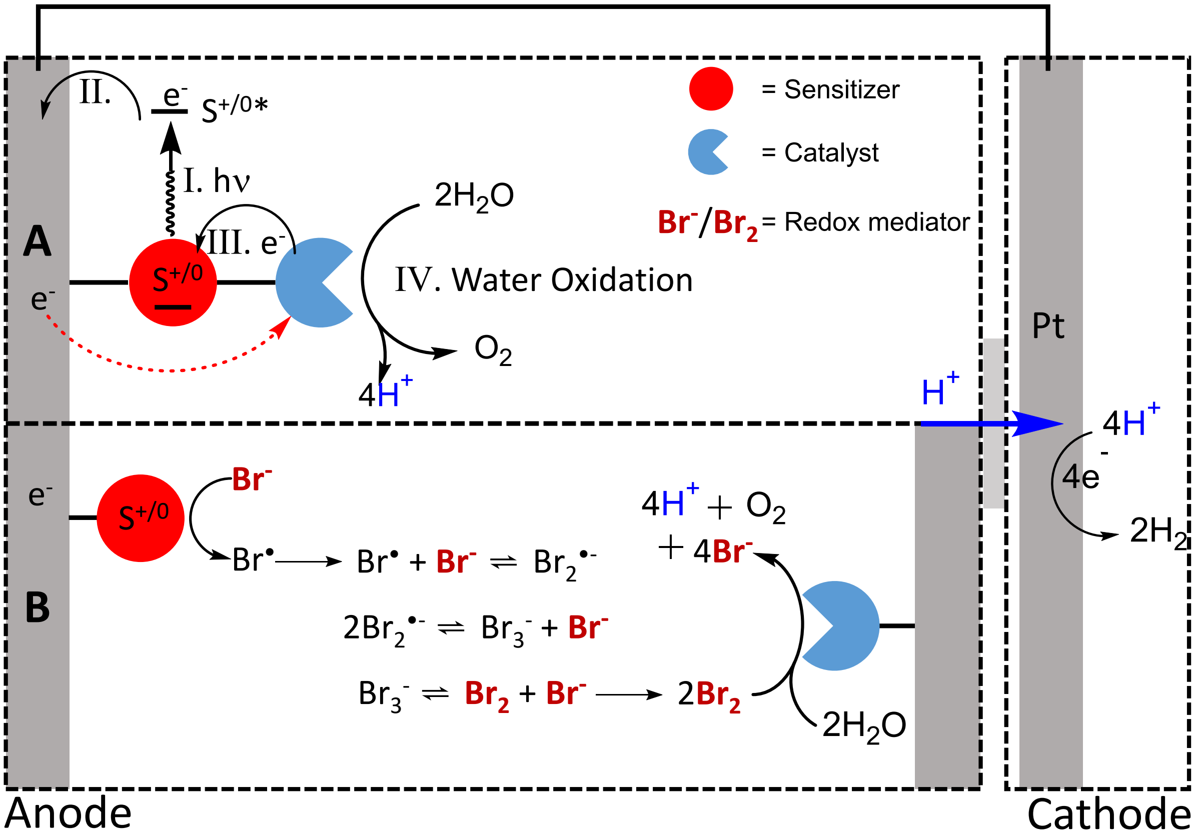

Figure 1. Dye-sensitized water splitting photoelectrosynthesis cells. The left half-cell shows the dye-sensitized processes that lead to water oxidation at the anode. The right half-cell depicts proton reduction at the cathode. (A) I. Photoexcitation of the sensitizer. II. Excited-state electron injection from the sensitizer to the semiconductor. III. Thermal electron transfer from the water oxidation catalyst to the sensitizer. IV. Water oxidation occurs after four oxidizing equivalents have been transferred to the catalyst. (B) After excited state injection, S^+ oxidizes bromide to yield the bromine atom, $Br^\cdot$. In acidic aqueous solutions concentrated with bromide ions, the photogenerated bromine atom reacts with Br^- to form dibromide, $Br_2^{\cdot -}$, that is unstable with respect to disproportionation to yield tribromide that is in equilibrium with elemental bromine, Br_2, that is thermodynamically competent of initiating water oxidation at a remote catalytic cite.

A challenge associated with dye-sensitized generation of strong oxidants at semiconductor interfaces is that S* must be a potent excited-state reductant, for quantitative electron injection, and S^+ must react with the mediator more rapidly than competitive back reaction. As was recently described, there is a delicate interplay between ground- and excited-state reduction potentials that make it difficult to tune both for optimal behavior while still maintaining light absorption throughout the visible region.[37]

A dual-sensitizer photoanode approach with a molecular catalyst has been reported for water oxidation,[34] but the conversion efficiencies were low even when losses associated with transmitted light were taken into account.[34] Herein is reported a mechanistic study designed to identify loss mechanism(s) in the dual-sensitizer approach. Two sensitizers were utilized that have favorable energetics for inter-sensitizer electron transfer, Figure 2. The sensitizer **Org** is linked directly to rutile core/shell SnO_2/TiO_2 nanoparticles in a mesoporous thin film (~50 µm) photoanode. An Al_2O_3 overlayer stabilizes **Org** and provides a binding site for a second sensitizer, **Ru**. The desired sequence of electron transfer reactions are as follows. Upon blue light absorption **Org*** injects an electron into the core-shell nanoparticle thin film. Longer wavelength light absorption creates **Ru*** that reduces **Org°**. The **Ru^{ox}** intermediate then oxidizes bromide at the aqueous electrolyte interface. Time resolved anisotropy measurements indicated that the Ru* undergoes lateral intermolecular energy transfer across oxide surfaces and with Monte-Carlo simulations provided a rate constant. In addition, an unproductive excited-state electron transfer pathway was identified that lowers the efficiency. This fundamental research shows that a dual-sensitizer photoanode is indeed capable of generating Br_2 that is known to mediate water oxidation catalysis.[35]

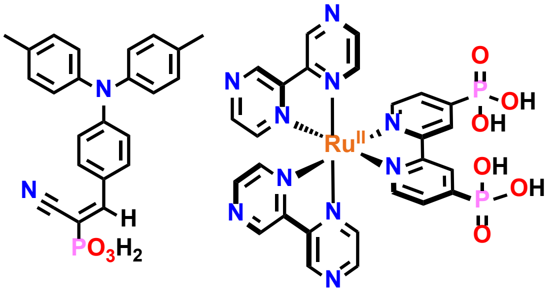

Org **Ru**

Figure 2: Structures and abbreviations of the sensitizers utilized herein.

Experimental

Materials. Sodium Acetate (Sigma-Aldrich, ≥99%), glacial acetic acid (Fisher, certified ACS), sodium bromide (EM Science), and sodium perchlorate (Acros Organics, 98%), were used as received. Argon gas (Airgas, 99.998%) was passed through a Drierite drying tube before use. All solvents were ACS grade and used as received. The two sensitizers, **Org** and **Ru** were available from previous studies. Fluorine-doped tin oxide (FTO) was purchased from Hartford Glass (15 Ω/sq).

Thin Film Preparation. The mesoporous thin films SnO_2/TiO_2 core/shell[33] and ZrO_2[38] were prepared as was previously reported from colloidal SnO_2 or ZrO_2 solutions. The SnO_2 or ZrO_2 solutions were doctor bladed onto a methanol-cleaned FTO glass substrate using Scotch tape

(~50 μm thick). The doctor bladed films were covered and allowed to dry at room temperature for 30 min, then heated for 30 min at 450 °C under an O_2 atmosphere (~1 atm). These films were then stored in a ~70 °C oven until use. The thin films were placed in ~1 mM **Org** methanol solution and allowed to react for at least 48 hours. Prior to use, films were rinsed with neat MeOH. The dual-sensitizer CS|**Org**|Al_2O_3|**Ru** was prepared by first reacting **Org** with the SnO_2/TiO_2 core/shell films and subsequent atomic layer deposition (see below) of Al_2O_3 followed by a 48 hr reaction in a ~1 mM **Ru** methanol solution.

Atomic Layer Deposition. Atomic layer deposition (ALD) was performed in a commercial reactor (Savannah S200, Cambridge Nanotech). The core/shell SnO_2/TiO_2 films were prepared by atomic layer deposition of TiO_2 onto the SnO_2 films using tetrakis-dimethyl amine titanium, (TDMAT), held at 75 °C, and water as the precursors. The deposition conditions were 130 °C under 20 sccm carrier N_2 gas. An ALD "cycle" consisted of a 1 s TDMAT pulse, 15 s hold, 50 s N_2 purge, 0.02 s H_2O pulse, 15 s hold, and 50 s N_2 purge. These core/shell thin films were annealed for 30 min under an O_2 flow at 450 °C.

Aluminum oxide (Al_2O_3) was deposited using trimethylaluminum (TMA). The reactor temperature was held at 130 °C, whereas the TMA reservoir was kept at room temperature. The TMA was pulsed into the reactor for 0.02 s and then held for 30 s before opening the pump valve and purging for 35 s. ALD coating conditions were 130 °C with a 20 sccm N_2 carrier gas flow rate with a sequence of 0.02 s TMA dose, 30 s hold, 35 s N_2 purge, 0.02 s H_2O dose, 30 s hold, 35 s N_2 purge for 10 cycles, with ~1.1 Å Al_2O_3 deposited per cycle.

Spectroscopy.

UV−Visible Absorption. All steady-state UV− visible absorption spectra were obtained on an Agilent Cary 60 spectrophotometer at room temperature in 1.0 cm path length cuvettes. The functionalized thin films were placed diagonally in the cuvettes at a 45° angle to the probe light.

Nanosecond Transient Absorption. Nanosecond transient absorption measurements were obtained with an apparatus that has previously been described.[39] Briefly, samples were excited by a Q-switched, pulsed Nd:YAG laser (Quantel U.S.A. (Big Sky) Brilliant B; 5−6 ns full width at half-maximum (fwhm)) tuned to 532 nm or 488 nm light from an optical parametric oscillator (OPO, Opotek, Inc.). The excitation irradiance was typically 3−5 mJ/pulse as measured by a Thor Laboratories PM100D laser power meter. The laser beam was directed 45° to the film surface. A 150 W Xe arc lamp served as the probe beam and was aligned orthogonal to the laser excitation light. The probe lamp was pulsed for measurements on sub-100 μs time scales. Detection was achieved with a monochromator (SPEX 1702/04) optically coupled to an R928 photomultiplier tube (Hamamatsu). Transient data were acquired with a computer-interfaced digital oscilloscope (LeCroy 9450, Dual 330 MHz) with an overall instrument response time of ∼10 ns. Typically, 30-90 laser pulses were averaged at each observation wavelength over the range 390−760 in 10 nm intervals. Full spectra were generated by averaging 2−10 points on either side of the desired time value to reduce noise in the raw data.

Data Analysis. Data fitting was performed in OriginPro 2017, with least-squares error minimization achieved using the Levenberg−Marquardt method. The errors reported for fitting parameters are the standard errors.

Nanosecond Transient Anisotropy. Nanosecond transient anisotropy data were obtained with the transient absorption described. The probe light was directed through a 1/4 m monochromator (Spectral Energy Corp., GM 252) before the sample. All measurements utilized a Glan−Taylor polarizer (Thorlabs, GL 10-A) for excitation (Pex) and a second Glan−Taylor polarizer (Pdet) for the probe beam. For anisotropy measurements, Pex was set to vertical, the same polarization as the laser, and Pdet was set to either vertical (V) or horizontal (H). Magic angle and anisotropy values were calculated via eqs 1 and 2, respectively:

$$\Delta\, Abs_{magic\ angle} = \frac{(VV+2VH)}{3} \qquad (1)$$

$$r = \frac{(VV-VH)}{3\Delta Abs_{magic\ angle}} \qquad (2)$$

where VY is the change in absorbance observed with excitation polarization V and detection polarization Y = V or H and r is the anisotropy value. Typically, 60 laser pulses were averaged at each observation wavelength and 5−10 identical measurements were taken and averaged to help increase the signal-to-noise ratio of the anisotropy data.

Simulations of Anisotropy Data. Monte Carlo simulations were employed to simulate the anisotropy decays measured after vertical polarized light excitation. The simulation utilized a 20 nm spherical nanocrystallite with sensitizers spaced at approximately the intermolecular distance, δ, extracted from surface coverage measurements, vide infra. The simulated sensitizers were distributed across the nanoparticle surface through an iterative Coulomb's law force minimization, which produced a nearly even sensitizer distribution. To simulate the low laser power utilized experimentally, one excited state was generated per nanocrystallite for each simulation. The probability of an excited state being generated at a specific location was proportional to $\cos^2 \varphi$, where φ is the inclination angle of the vertical plane, i.e., vertically polarized light has $\varphi = 0$. For each initialization, the excited-state sensitizer generated after vertically polarized excitation was assumed to quantitatively inject an electron. After formation of the oxidized sensitizer, or hole, a random-walk simulation was performed. For each sensitizer, 10000 random walks consisting of 1000 iterations were averaged to determine the simulated anisotropy decay as a function of the iteration step. Self-exchange electron transfer was modeled with an exponential distance dependence for the probability of transfer with $\beta = 1.2$ Å^{-1}, as previously determined.[40] The anisotropy, r, at any time during the random walk was calculated via eq 3, where $\langle \cos^2 \varphi \rangle$ was the average of the square of the cosine of the inclination angle of the oxidized sensitizer position.

$$r = \frac{3\langle cos^2 \varphi \rangle - 1}{2} \tag{3}$$

With the time per iteration step as the only adjustable parameter, the experimentally determined anisotropy decays were modeled directly with the simulated anisotropy decays. The best fit with respect to time per iteration was then utilized to determine the resulting self-exchange rate constant, k_{MC}, for each sensitizer. The Monte Carlo simulations were performed with Wolfram Mathematica 11.0.1.0.

Photoelectrochemical Cells. Photocurrent measurements were performed on a BASi Epsilon potentiostat with a standard three-electrode configuration (working electrode, photocatalyst sensitized SnO_2/TiO_2 core/shell on FTO with 500 mV applied potential; reference electrode, Ag/AgCl (4 M KCl, externally referenced to SCE); counter electrode, Pt mesh) in a custom-built H-cell with the two half-cells separated by a Nafion proton-exchange membrane. **White Light Illumination**. Under white light illumination from a Cole Parmer 41720-Series fiber optic illuminator, thin film slides were positioned to receive 100 mW cm^{-2} as determined with a Coherent Molectron PM 5200 laser power meter. A 400 nm long-pass filter was used to inhibit direct bandgap excitation of the metal oxide layer. The geometric area of the photoanode was used for reporting current densities. Unless otherwise stated, solutions were sparged with argon for 30 min prior to experiment.

Incident and Absorbed Photon-to-Current Efficiencies (IPCE and APCE). For monochromatic light excitation, a Coherent Genesis MX 460 or 532 nm solid-state laser was utilized as the illumination source with photon output calibrated using a Thor Laboratories PM100D laser power meter. Photocurrents were measured as a function of the excitation irradiance. The reported IPCE and APCE values were calculated with a laser power of 20 mW cm^{-2}. For all experiments utilizing an applied potential, a Ag/AgCl reference electrode externally calibrated to a SCE electrode (241 mV vs NHE) was used. All potentials are reported versus NHE.

Faradaic Efficiency. The Faradaic efficiency was quantified with coulometric determination of the number of electrons in the integrated photocurrent and spectroscopic determination of the number of Br_2 and Br_3^- generated. The tribromide (Br_3^-) and bromine (Br_2), are in equilibrium, Equation 4.[36,37]

$$Br^- + Br_2 \rightleftharpoons Br_3^- \qquad\qquad K_{eq} = 16 \qquad (4)$$

The known extinction coefficient of Br_3^- (ε(266 nm) = 40900 M^{-1} cm^{-1})[36] and the equilibrium constant, the total photoproduct concentration was calculated. Thin film photoanodes immersed in a known volume of pH 4.76 solution (0.2 M acetate buffer, 0.3 M NaBr) were illuminated with 460 nm steady-state illumination for fixed periods of time (**Figure S1**, left). After illumination, an aliquot of the electrolyte solution was removed and the absorption spectrum was measured (**Figure S1**, right). The ratio of oxidized bromide photoproducts to the total charge passed during illumination while taking into account the 2-electron oxidation provided a Faradaic efficiency of 14% for CS|**Org**|Al_2O_3|**Ru**. In the control experiment with CS|**Org** where the laser power was attenuated to give the same photocurrent magnitude, no Br_3^- photoproduct was observed over the same time frame (**Figure S2**).

Results

The two sensitizers utilized (1-cyano-2-(4-(di-p-tolylamino)phenyl)vinyl)phosphonic acid (**Org**) and $[Ru(bpz)_2(4,4'-(PO_3H_2)_2-2,2\text{-bipyridine}]^{2+}$ (**Ru**) (Figure 2), have been previously reported.[37,41] The CS|**Org**|Al_2O_3|**Ru** thin films were prepared sequentially starting with mesoporous SnO_2|TiO_2 core/shell (CS) thin films functionalized with **Org**. Atomic layer deposition (ALD) of an ~11 Å insulating Al_2O_3 overlayer yielded CS|**Org**|Al_2O_3 that was reacted with **Ru** to yield CS|**Org**|Al_2O_3|**Ru**.

The UV-visible absorption spectra of **Org** and **Ru** in methanol solutions are shown in Figure 3A. The relevant ground- and excited-state reduction potentials are reported in Table 1. The absorption spectrum of CS|**Org**|Al_2O_3|**Ru** and CS|**Org** are shown in Figure 3B. Notably, subtraction of the spectra of CS|**Org** from CS|**Org**|Al_2O_3|**Ru** results in a broad band at 465 nm, consistent with the presence of the metal-to-ligand charge-transfer (MLCT) absorption spectrum of **Ru**, Figure 3B inset. Significant broadening of the **Org** and **Ru** absorption spectra were observed for the sensitized oxide materials relative to solution . The spectroscopically determined surface coverages (Γ_0) were calculated with Equation 5, where A is the absorbance at λ_{max} and ε is the molar extinction coefficient. Surface coverages were 4.3 and 3.7×10^{-8} mol/cm^2 for **Org** and **Ru**, respectively.

$$A = 1000 \times \Gamma_0 \times \varepsilon \tag{5}$$

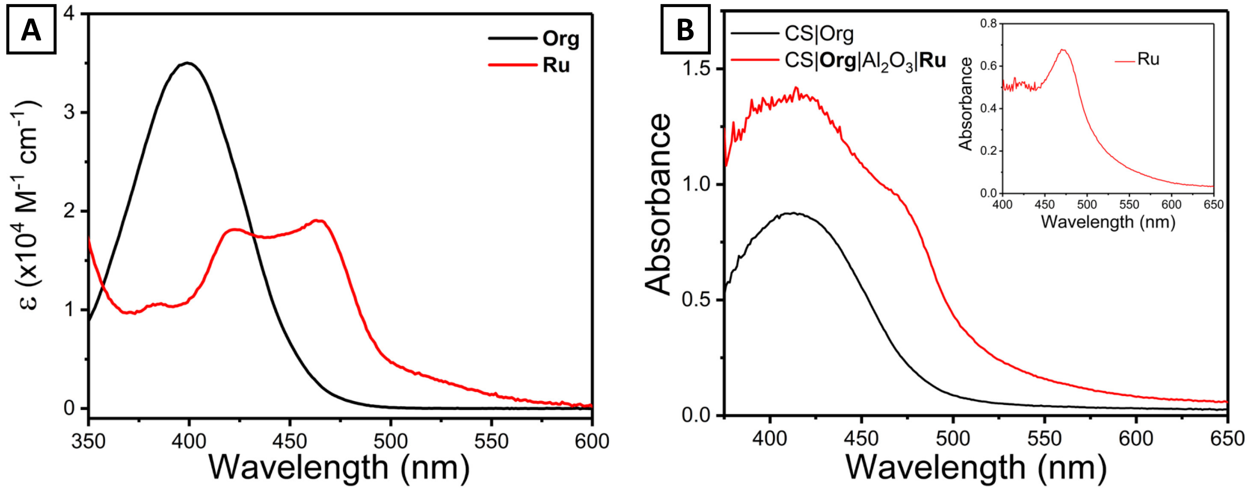

Figure 3. (A) UV-Visible absorption spectra of **Org** (black) and **Ru**(red) in MeOH solution. (B) UV-Visible absorption spectra of the CS|**Org** (black) and CS|**Org**|Al_2O_3|**Ru** (red) photoanodes. The inset shows the spectrum obtained by subtraction of the CS|**Org** spectrum from that of CS|**Org**|Al_2O_3|**Ru**.

Table 1. Absorption and Electrochemical Characterization of **Org** and **Ru**

	λmax (ε×10^4 M^{-1} cm^{-1})	E° ($S^{*0/+}$)	E° ($S^{0/+}$)
Org	400 nm (3.5)	-1.88	0.99
Ru	465 nm (1.9)	-0.25	1.85

Excited-State Electron Injection

Pulsed 488 nm laser excitation of CS|**Org** resulted in an absorption feature centered at 700 nm corresponding to $\textbf{Org}^{ox}$ (Figure S3).[41] This transient feature formed within the instrument response time, consistent with $k_{inj} > 10^8$ s^{-1}.[42,43] The kinetics for back-electron transfer (BET) from a CS electron to $\textbf{Org}^{ox}$ monitored at 700 nm (Figure S4) were nonexponential and successfully modeled by the Kohlrausch−Williams−Watts (KWW) function give by Equation 6, where A_0 is the initial amplitude, k_{obs} is the characteristic rate constant, and β is inversely proportional to the width of an underlying Lévy distribution. The average rate constant was determined with Equation 7 (where Γ is the gamma function), yielding a rate constant for $k_{KWW} = 5\times10^{2}$ s^{-1}.

$$\mathrm{Abs(t)} = \mathrm{A_0}\mathrm{e}^{-(k_{\mathrm{obs}}\mathrm{t})^{\beta}} \tag{6}$$

$$k_{\mathrm{KWW}} = \frac{k_{\mathrm{obs}}\beta}{\Gamma\left(\frac{1}{\beta}\right)} \tag{7}$$

Intermolecular Energy Transfer

Light absorption by **Ru** yielded an MLCT excited state that was not quenched by the CS acceptor states. The fate of the excited state was probed by time-resolved absorption anisotropy, a technique that has recently been utilized to quantify lateral self-exchange reactions occurring on nanoparticle surfaces.[44–46] Initial studies were frustrated by a reductive quenching pathway (see below), so an insulating zirconium oxide (ZrO_2) mesoporous thin film was utilized, abbreviated ZrO_2|**Ru**. Vertically polarized 532 nm laser excitation produced the MLCT excited state that was detected with either vertically (VV) or horizontally (VH) oriented polarizers, Figure 4A. A time-resolved anisotropy resulted that was used to determine the anisotropy decay, Figure 4B.

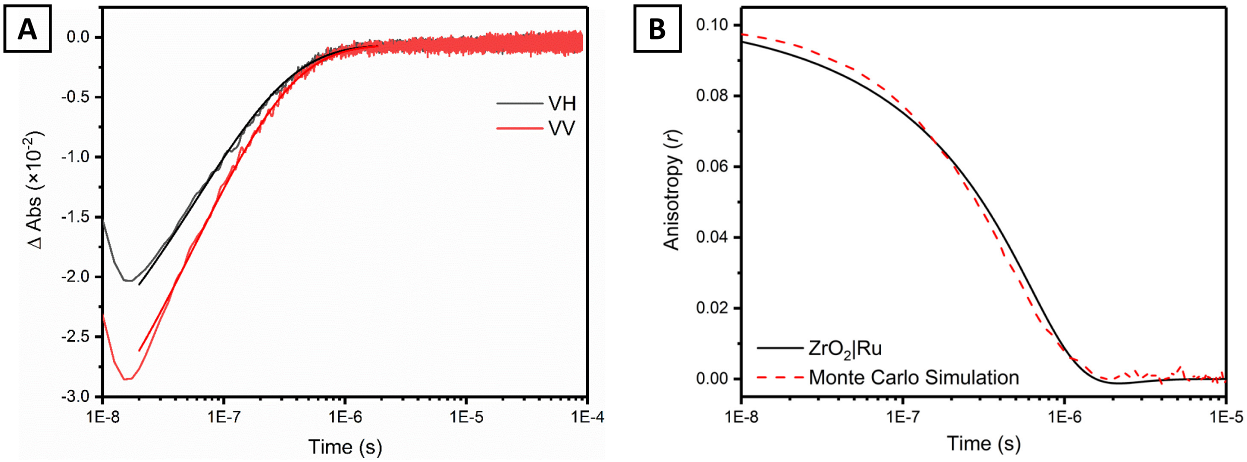

Figure 4. (A) Time-resolved absorption anisotropy decays measured after pulsed light excitation of ZrO_2|**Ru** with VV (red) and VH (black) polarization with overlaid fits. (B) The time resolved anisotropy (black) overlaid with the results of Monte Carlo simulations that provided an intermolecular energy transfer rate constant of 4×10^{7} s^{-1}.

The anisotropy decays wwe modeled with previously described Monte Carlo simulations.[45,46] An intermolecular energy transfer rate constant of 4×10^{7} s^{-1} was found that corresponds to ~ 25 ns per energy transfer consistent with reports of related ruthenium complexes, Figure 3B.[47] Therefore in the absence of excited state electron transfer, energy transfer occurs an average of 26 times within the excited state lifetime.

*Regeneration of **Ru**^{ox} with Br$^-$*

To test the utility of the CS|**Org**|Al_2O_3|**Ru** in generating strong oxidizing equivalents, the reaction of photogenerated **Ru**^{ox} with Br$^-$ was investigated. The formal one electron reduction potentials for Br$^{-/\bullet}$ and **Ru**$^{III/II}$ are 1.92 and 1.85 V vs. NHE, respectively.[36,37] Although Br$^-$ oxidation is unfavored by 70 meV, large rate constants have been previously reported when a large excess of Br$^-$ is present.[37,48] As prior reports show, **Ru*** is not a potent photoreductant and does not inject electrons into the CS acceptor states in the pH 4-6 range targeted for this study.[37] Therefore, mesoporous thin films of SnO_2 nanoparticles were utilized that possess more positive (on an electrochemical scale, i.e. further from the vacuum level) acceptor states. Pulsed 532 nm laser excitation of SnO_2|**Ru** anode resulted in a transient bleach at the 402 nm ground/excited-state isosbestic point (Figure 5, purple data), consistent with the formation of **Ru**^{ox}. This transient bleach was observed at both pH 4 and 5.6, indicated that **Ru*** injects an electron into SnO_2, yielding $SnO_2(e^-)$|**Ru**^{ox}

As shown in Figure 5, increased Br$^-$ concentrations resulted in faster **Ru**^{ox} regeneration. The kinetic data at each Br$^-$ concentration were successfully modelled by the KWW function. A plot of k_{KWW} verses the Br$^-$ concentration (Figure 5, inset) was linear with a slope that provided the regeneration rate constant k_{reg}= 2×10^7 M^{-1} s^{-1}.

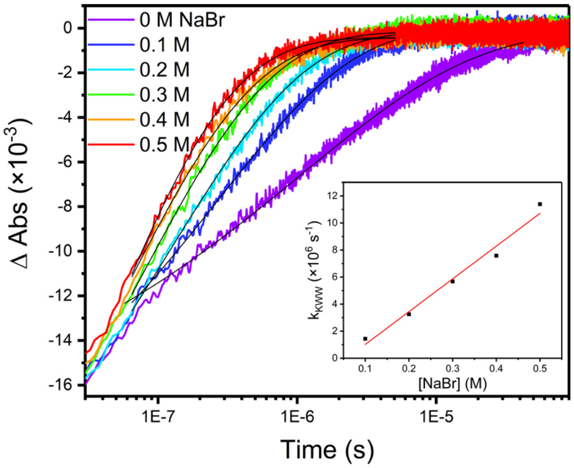

Figure 5. Regeneration of the oxidized ruthenium complex in pH 4 acetate buffer (0.2 M) with increasing Br$^-$ concentrations. The inset shows the observed rates verses the Br$^-$ concentration, the slope of which corresponds to the second order rate constant, $k_{reg,}$ = 2×10^7 M^{-1} s^{-1}.

Photocurrent Responses

To assess the performance of the dual-sensitizer photoanode for Br^- oxidation in pH 5.6 solutions, photocurrent measurements were obtained in a three electrode H-cell. The photoanode and reference electrode were placed in one compartment of the H-cell and illuminated with 100 mW cm^{-2} (1 sun), while a counter electrode was kept in a dark compartment. The photocurrent responses displayed an initial spike, that has previously been attributed to electrode polarization and fast electron transfer, followed by decay to a steady-state value.[12,27] In control experiments, white light excitation of CS|**Org** or CS|**Ru** photoanodes resulted in 40 or 2 μA cm^{-2} of sustained photocurrent, respectively. For the dual sensitizer CS|**Org**|Al_2O_3|**Ru**, 200 μA cm^{-2} of sustained photocurrent was measured indicating that the two sensitizers have a synergistic effect on the current output, Figure 6. A Faradaic yield for bromide oxidation of 14% was determined for CS|**Org**|Al_2O_3|**Ru.** In contrast, bromide oxidation products were not detected after illumination of CS|**Org**; a measurable decrease in the **Org** surface coverage suggested that the sensitizer itself was oxidized.

Incident and adsorbed photon-to-current efficiencies (IPCE and APCE) for Br^- were measured for the photoanode with 460 and 532 nm excitation in pH 4 solution (Figures S5 and S6, Table S1). As shown in Figure 3, both sensitizers absorb light at 460 nm, while only the ruthenium sensitizer absorbs significantly at 532 nm. The IPCE and APCE values were an order of magnitude greater with 460 nm excitation (IPCE = 1.2%, APCE = 1.4%) as compared to 532 nm excitation (IPCE = 0.08%, APCE = 0.13%), revealing that the photoanode efficiency decreases drastically when only the ruthenium sensitizer absorbed light. With 460 nm light excitation the photocurrent increased linearly with the light intensity.

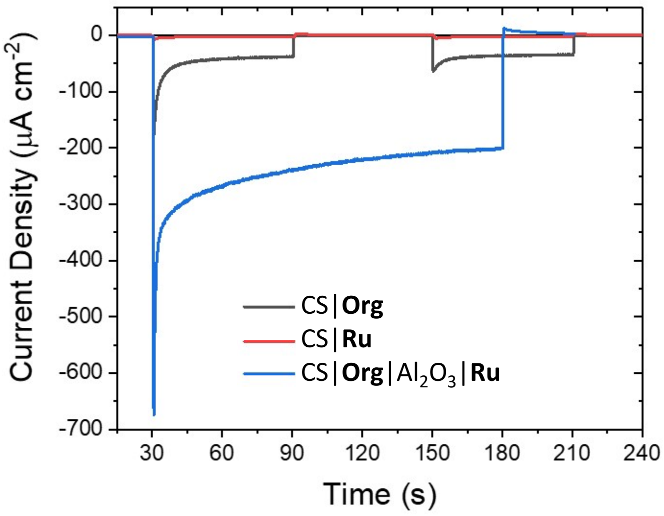

Figure 6. Light on/off current responses for CS|**Org** (black), CS|**Ru** (red), and CS|**Org**|Al$_2$O$_3$**Ru** (blue) photoanodes. The current responses were measured under 100 mW cm^{-2} white light illumination with a 0.5 V vs. NHE applied potential in 0.2 M acetate buffer (pH 5.6) and 0.3 M NaBr.

*Reductive Quenching of **Ru*** by **Org***

In the dual-sensitizer assembly, the IPCE and APCE values indicated that the efficiency of Br$^-$ oxidation was suboptimal.[37,48] This suggested the presence of a nonproductive electron transfer pathway. The absorption difference spectra measured after pulsed 488 or 532 nm excitation of MOx|**Org**|Al$_2$O$_3$|**Ru** (MOx = CS or TiO$_2$) revealed a positive absorption growth at 500 nm assigned to the reduced complex, **Ru**^{red},[49–51] and the characteristic absorption of **Org**^{ox} centered near 700 nm, Figure S7.

Additional insights were gained by successfully isolating this reaction through an alternative oxide design wherein a dual-sensitizer assembly was prepared with an insulating ZrO$_2$ core instead of the CS semiconductor, yielding the following structure, ZrO$_2$|**Org**|Al$_2$O$_3$|**Ru**. In this assembly, excited-state electron injection from **Org*** was not observed spectroscopically. Pulsed 532 nm excitation resulted in the appearance of absorption features at 500 and 700 nm, consistent with the formation of **Ru**^{red} and **Org**^{ox}, Figure 7A. Varying the Al$_2$O$_3$ layer thickness from 5.5 to 22 Å (5 – 20 cycles) was found to have a dramatic impact on the yield, Figure 7B. With thin shells (5.5 – 11 Å Al$_2$O$_3$), significant amplitude was apparent, but when the thickness was increased to 22 Å, the yield was near zero.

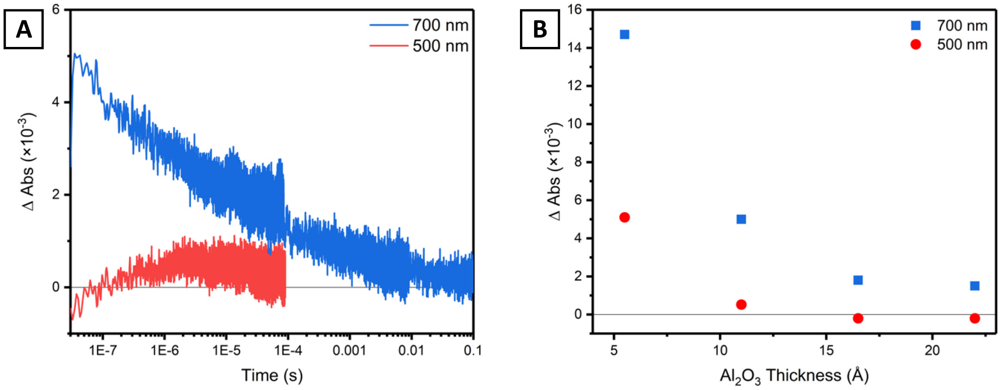

Figure 7. (A) Time-resolved absorption changes at 500 (red) and 700 (blue) nm upon 532 nm excitation of ZrO_2|**Org**|Al_2O_3**Ru** anodes in 0.2 M acetate buffer (pH 5.6). (B) The maximum amplitude change for the absorption monitored at 500 and 700 nm versus the thickness of the insulating Al_2O_3 layer.

Discussion

Dye-sensitized Br^- oxidation with a dual-sensitizer photoanode design has been realized in pH 5.6 aqueous solution. Previous research has been limited to organic solvents or highly acidic (pH 0-1) aqueous solutions, conditions that simplify many of the challenges associated with dye-sensitized Br^- oxidation. For instance, the $Br^{\bullet/-}$ potential is less positive in organic solvents (1.42 V vs NHE in acetone)[52] as compared to water (1.92 V vs NHE),[53] allowing weaker ground-state oxidants for catalysis.[54,55] In aqueous electrolytes, acid shifts the semiconductor acceptor states to lower energy (i.e. away from the vacuum level), facilitating excited-state injection. While excitation wavelength dependent photocurrent measurements indicate an advantage of the dual-sensitizer photoanode design, the Faradaic yields of Br_2/Br_3^- were only about 14% indicating that other oxidation reactions were operative. In addition, the overall photocurrent on an absorbed photon-to-current efficiency was less than 2% implying that unproductive recombination pathway(s) were operative that were indeed identified by transient absorption spectroscopy as described below.

A generalized depiction of the dual-sensitizer photoanode is shown in the left panel of Figure 8. The photoanode was designed so that the inner sensitizer (**Org**) was a potent photoreductant positioned for excited-state electron injection, while the outer sensitizer (**Ru**) was a potent oxidant present at the electrolyte interface for Br^- oxidation. In the right panel of Figure 8, the desired processes for an operational HBr splitting cell are plotted on an energy axis. This represents a Z-type scheme. The artificial Z-scheme is applied here to two molecular sensitizers whereas previous reports have utilized two light absorbing semiconductors[56–60] or a semiconductor with a single sensitizer.[61,62] For CS|**Org**|Al_2O_3|**Ru**, blue light ($h\nu_1$) absorbed by **Org** yields an electronic excited-state **Org*** that quantitatively injects an electron into the core/shell metal oxide. Green light ($h\nu_2$) excites the outer **Ru** sensitizer and yields an MLCT excited-state **Ru*** that undergoes excited-state energy transfer across the oxide surface until it encounters $\mathbf{Org^{ox}}$. A large driving force (1.24 V) for the electron-transfer reaction ($k_{reg,1}$), $\mathbf{Org^{ox}} + \mathbf{Ru}^{*} \rightarrow \mathbf{Org} + \mathbf{Ru^{ox}}$ translates the oxidizing equivalent to $\mathbf{Ru^{ox}}$ present at the electrolyte interface. Despite a strong thermodynamic driving force for this reaction, $-\Delta G^{o} = 1.24$ eV, it was not efficient in the photoelectrochemical cells. Excited state injection was quantitative and Br^- oxidation occurred with a large rate constant $k_{reg} = 2\times10^{7}\ M^{-1}\ s^{-1}$, however the measured photocurrents were far from optimal.

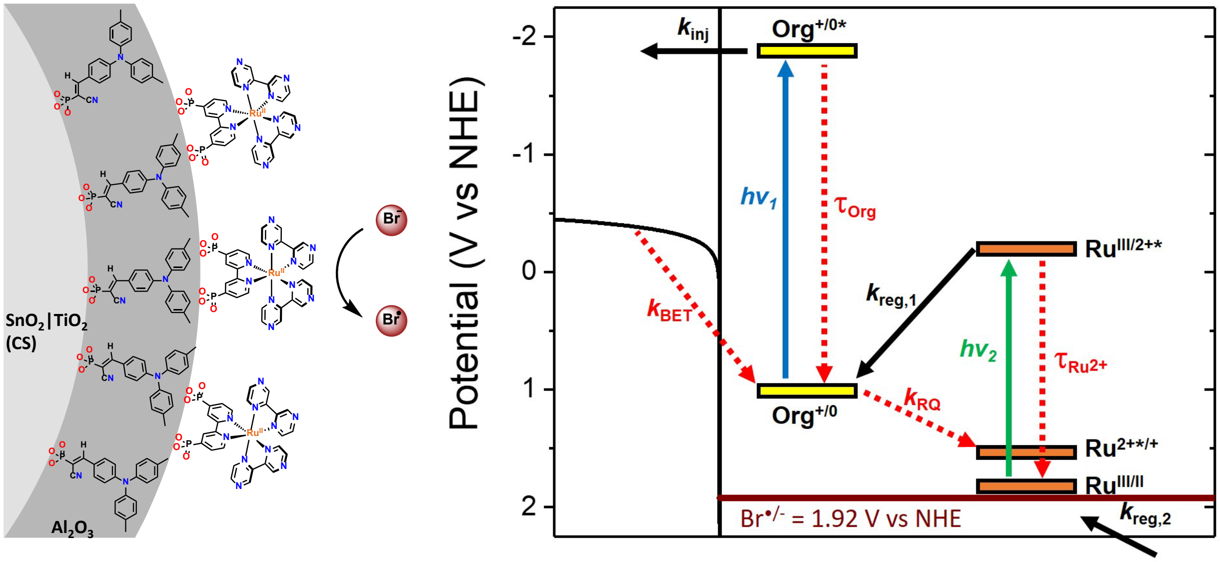

Figure 8. A depiction of the dual-sensitizer photoanode used for bromide oxidation at pH 4-6 (left panel). The right panel shows the proposed electron transfer reactions (beneficial in solid arrows, non-beneficial in dashed arrows) on an energy axis.

In addition to the desired electron transfer reactions, a variety of non-productive pathways (right panel Figure 8, dashed arrows) are possible. Despite a short < 1 ns **Org** excited-state lifetime, excited-state injection quantum yields of unity were obtained.[41] The $\mathbf{Ru}^{*}$excited-state lifetime of $\tau = 0.67\ \mu s$ is approximately three orders of magnitude longer than that of **Org**, yet $\mathbf{Ru}^{*}$ did not undergo measureable excited state injection; behavior attributed to weak electronic coupling to the core/shell oxide and to a low thermodynamic driving force. Instead, the $\mathbf{Ru}^{*}$ excited state undergoes lateral intermolecular energy transfer across the insulating interface. Monte-Carlo simulations indicated that on average the Ru* ‘hops’ to a neighbor sensitizer 26 times before relaxation to the ground state. Such energy migration is proposed to increase the likelihood that **Ru*** encounters **Org^{ox}**. In principle, the **Org^{ox}** could undergo lateral **Org^{ox}/Org** self-exchange, often called hole-hopping.[63,64] However, prior research has shown that lateral electron transfer is inhibited when sensitizers are buried in Al_2O_3 overlayers.[46,65] Hence **Ru*** energy transfer to the **Org*** injection site, or the statistical photo-creation of proximate **Ru*** and **Org***, provide the likely mechanisms for bromide oxidation prior to back electron transfer that occurred with an average rate constant of k_{BET}= 5×10^2 s^{-1}.

The energy diagram of Figure 8 shows a significant driving force for reductive quenching (500 meV) of **Ru*** by ground state **Org** (**Org** + **Ru*** → **Org$^+$** + **Ru^{red}**) with a rate constant k_{RQ}. To determine whether this non-beneficial pathway was operative under normal cell conditions, a related oxide structure was prepared, in which an insulating metal oxide ZrO_2 was employed to create a ZrO_2|**Org**|Al_2O_3|**Ru** structure. The acceptor states of ZrO_2 are high in energy and preclude **Org*** excited-state electron injection. In the absence of excited state injection, **Ru*** was indeed quenched by Org by reductive electron transfer to yield **Org^{ox}** that returned to ground state products on a millisecond time scale

In principle this non-productive rate constant k_{RQ} could be controlled through the driving force for electron transfer ($-\Delta G^o$), the reorganization energy (λ), and/or the electronic coupling (H_{AB}) between the two sensitizers. Increasing the thickness of the Al_2O_3 overlayer was found to have a large impact on the yield, presumably through decreased electronic coupling, due to the larger distance between the **Org** and **Ru** sensitizers,[66] and an increase reorganization energy as the insulating overlayer inhibits solvents and ion motion.[67,68] In anodes with thin insulating layers (5.5 and 11 Å), both **Org^{ox}** and **Ru^{red}** were observed transiently. However, the concentration of products from the reductive quenching reaction were significantly less when an 11 Å Al_2O_3 layer was present relative to a 5.5 Å layer. As the Al_2O_3 thicknesses was increased from 16.5 to 22 Å, the yield of reductive quenching plateaued, with only a small concentration of **Org$^+$** being resolved. In future research, it will be of interest to examine whether these thick Al_2O_3 overlayers also inhibit the desired **Ru*** + **Org^{ox}** → **Ru**^{ox} + **Org** reaction. The use of alternative sensitizers, particularly a weaker oxidant as the inner-sensitizer, would lower the reaction free energy change resulting in enhanced bromide photo-oxidation efficiency.

Conclusions

The photo-generation of the strong oxidant Br_2 has been achieved at a metal oxide/ electrolyte interface a dual-sensitizer photoanode design. This advance enhances the scope of dye-sensitized bromide oxidation from organic solvents and strongly acidic solutions to mildly acidic aqueous conditions (pH 5.6) where the kinetics for water oxidation catalysis are more ideal. The use of two sensitizers in an artificial z-scheme was found to simplify several of the challenges associated with photocatalytic bromide oxidation. First, the inclusion of two sensitizers allowed the properties of each sensitizer to be tuned for its specific task ensuring near unity injection and large rate constants for bromide oxidation. This removed the necessity of finding a single sensitizer that was best able to balance these parameters. Second, the use of Br^- as a redox mediator ($E^o(Br^{-/\bullet})$ = 1.92 V vs. NHE) allows favorable disproportionation and equilibrium chemistry to be exploited, as the oxidized mediator ($Br^\bullet$) is known to yield Br_2 in bromide-containing acidic aqueous and organic solutions. The disadvantage of this strategy is that two photons are required to generate an injected electron and a Br instead of one. This stands in contrast to prior approaches that utilized a single chromophore, where it was necessary to balance the ground- and excited-state redox potentials so that both electron injection and bromide oxidation could be achieved.

This dual-sensitizer photoanode is ripe for further investigations. The modular design of the anode allows sensitizers to be chosen that have complimentary absorption spectra, such that more significant portions of the solar spectrum can be harvested. Optimization of intermolecular energy transfer and hole-hopping to enhance encounters between **Ru*** and **Org^{ox}** provide a rational means to improve efficiency. The mechanistic study here reveals that efficient bromide oxidation requires an inner-sensitizer that is a weaker oxidant so as to prevent unwanted reduction of the outer sensitizer excited state. Dye-sensitized bromide oxidation to yield a $Br^\bullet$ atom undergoes a disproportionation like reaction that yields Br_2 that is a known redox mediator for water oxidation. Hence single photon one-electron transfer oxidations can drive the demanding multi-electron and multi-proton oxidation of water.

Supporting Information. Transient absorption and kinetic data are included as well as photocurrents measured with blue and green light.

Acknowledgements.

This research is supported by the National Science Foundation (NSF) under Award Number 1800022. This work made use of atomic layer deposition instrumentation at the Chapel Hill Analytical and Nanofabrication Laboratory (CHANL), a member of the North Carolina Research Triangle Nanotechnology Network (RTNN), which is supported by the National Science Foundation (Grant ECCS-1542015) as part of the National Nanotechnology Coordinated Infrastructure (NNCI). M.D.T. would like to acknowledge the NSF Graduate Research Fellowship Program under Grant No. DGE-1650116 for support.

References

(1) Brennaman, M. K.; Dillon, R. J.; Alibabaei, L.; Gish, M. K.; Dares, C. J.; Ashford, D. L.; House, R. L.; Meyer, G. J.; Papanikolas, J. M.; Meyer, T. J. Finding the Way to Solar Fuels with Dye-Sensitized Photoelectrosynthesis Cells. *J. Am. Chem. Soc.* **2016**, *138*, 13085–13102.

(2) Song, W.; Chen, Z.; Brennaman, M. K.; Concepcion, J. J.; Patrocinio, A. O. T.; Iha, N. Y. M.; Meyer, T. J. Making solar fuels by artificial photosynthesis. *Pure Appl. Chem.* **2011**, *83*, 749–768.

(3) Ashford, D. L.; Gish, M. K.; Vannucci, A. K.; Brennaman, M. K.; Templeton, J. L.; Papanikolas, J. M.; Meyer, T. J. Molecular Chromophore−Catalyst Assemblies for Solar Fuel Applications. *Chem. Rev.* **2015**, *115*, 13006–13049.

(4) Alibabaei, L.; Luo, H.; House, R. L.; Hoertz, P. G.; Lopez, R.; Meyer, T. J. Applications of metal oxide materials in dye sensitized photoelectrosynthesis cells for making solar fuels: let the molecules do the work. *J. Mater. Chem. A* **2013**, *1*, 4133–4145.

(5) Youngblood, W. J.; Lee, S.-H. A.; Maeda, K.; Mallouk, T. E. Visible Light Water Splitting Using Dye- Sensitized Oxide Semiconductors. *Acc. Chem. Res.* **2009**, *42* (12), 1966–1973.

(6) Swierk, J. R.; Mallouk, T. E. Design and development of photoanodes for water-splitting dye-sensitized photoelectrochemical cells. *Chem. Soc. Rev.* **2013**, *42*, 2357–2387.

(7) Xu, P.; McCool, N. S.; Mallouk, T. E. Water splitting dye-sensitized solar cells. *Nano Today* **2017**, *14*, 42–58.

(8) Young, K. J.; Martini, L. A.; Milot, R. L.; Snoeberger III, R. C.; Batista, V. S.; Schmuttenmaer, C. A.; Crabtree, R. H.; Brudvig, G. W. Light-driven water oxidation for solar fuels. *Coord. Chem. Rev.* **2012**, *256*, 2503–2520.

(9) Berardi, S.; Drouet, S.; Francas, L.; Gimbert-Surinach, C.; Guttentag, M.; Richmond, C.; Stoll, T.; Llobet, A. Molecular artificial photosynthesis. *Chem. Soc. Rev.* **2014**, *43*, 7501–7519.

(10) Yu, Z.; Sun, L. Recent advances in dye-sensitized photoelectrochemical cells for solar hydrogen production based on molecular components. *Energy Environ. Sci.* **2015**, *8*, 760–775.

(11) Youngblood, W. J.; Lee, S.-H. A.; Kobayashi, Y.; Hernandez-Pagan, E. A.; Hoertz, P. G.; Moore, T. A.; Moore, A. L.; Gust, D.; Mallouk, T. E. Photoassisted Overall Water Splitting

in a Visible Light-Absorbing Dye-Sensitized Photoelectrochemical Cell. *J. Am. Chem. Soc.* **2009**, *131*, 926–927.

(12) Zhao, Y.; Swierk, J. R.; Megiatto, J. D.; Sherman, B.; Youngblood, W. J.; Qin, D.; Lentz, D. M.; Moore, A. L.; Moore, T. A.; Gust, D.; Mallouk, T. E. Improving the efficiency of water splitting in dye-sensitized solar cells by using a biomimetic electron transfer mediator. *Proc. Natl. Acad. Sci. U. S. A.* **2012**, *109* (39), 15612–15616.

(13) Alibabaei, L.; Brennaman, M. K.; Norris, M. R.; Kalanyan, B.; Song, W.; Losego, M. D.; Concepcion, J. J.; Binstead, R. A.; Parsons, G. N.; Meyer, T. J. Solar water splitting in a molecular photoelectrochemical cell. *Proc. Natl. Acad. Sci. U. S. A.* **2013**, *110*, 20008–20013.

(14) Alibabaei, L.; Sherman, B. D.; Norris, M. R.; Brennaman, M. K.; Meyer, T. J. Visible photoelectrochemical water splitting into H_2 and O_2 in a dye-sensitized photoelectrosynthesis cell. *Proc. Natl. Acad. Sci. U. S. A.* **2015**, *112*, 5899–5902.

(15) Sherman, B. D.; Ashford, D. L.; Lapides, A. M.; Sheridan, M. V; Wee, K. R.; Meyer, T. J. Light-Driven Water Splitting with a Molecular Electroassembly-Based Core/Shell Photoanode. *J. Phys. Chem. Lett.* **2015**, *6*, 3213–3217.

(16) Moore, G. F.; Blakemore, J. D.; Milot, R. L.; Hull, J. F.; Song, H.; Cai, L.; Schmuttenmaer, C. A.; Crabtree, R. H.; Brudvig, G. W. A visible light water-splitting cell with a photoanode formed by codeposition of a high-potential porphyrin and an iridium water-oxidation catalyst. *Energy Environ. Sci.* **2011**, *4*, 2389–2392.

(17) Yamamoto, M.; Wang, L.; Li, F.; Fukushima, T.; Tanaka, K.; Sun, L.; Imahori, H. Visible light-driven water oxidation using a covalently-linked molecular catalyst–sensitizer dyad assembled on a TiO_2 electrode. *Chem. Sci.* **2016**, *7*, 1430–1439.

(18) Sherman, B. D.; Xie, Y.; Sheridan, M. V; Wang, D.; Shaffer, D. W.; Meyer, T. J.; Concepcion, J. J. Light-Driven Water Splitting by a Covalently Linked Ruthenium-Based Chromophore− Catalyst Assembly. *ACS Energy Lett.* **2017**, *2*, 124–128.

(19) Swierk, J. R.; McCool, N. S.; Saunders, T. P.; Barber, G. D.; Strayer, M. E.; Vargas-Barbosa, N. M.; Mallouk, T. E. Photovoltage Effects of Sintered IrO_2 Nanoparticle Catalysts in Water-Splitting Dye-Sensitized Photoelectrochemical Cells. *J. Phys. Chem. C* **2014**, *118*, 17046–17053.

(20) Swierk, J. R.; Méndez-Hernádez, D. D.; McCool, N. S.; Liddell, P.; Terazono, Y.; Pahk, I.;

Tomlin, J. J.; Oster, N. V; Moore, T. A.; Moore, A. L.; Gust, D.; Mallouk, T. E. Metal-free organic sensitizers for use in water-splitting dye-sensitized photoelectrochemical cells. *Proc. Natl. Acad. Sci. U. S. A.* **2015**, *112* (6), 1681–1686.

(21) Li, L.; Duan, L.; Xu, Y.; Gorlov, M.; Hagfeldt, A.; Sun, L. A photoelectrochemical device for visible light driven water splitting by a molecular ruthenium catalyst assembled on dye-sensitized nanostructured TiO_2. *Chem. Commun.* **2010**, *46*, 7307–7309.

(22) Gao, Y.; Ding, X.; Liu, J.; Wang, L.; Lu, Z.; Li, L.; Sun, L. Visible Light Driven Water Splitting in a Molecular Device with Unprecedentedly High Photocurrent Density. *J. Am. Chem. Soc.* **2013**, *135*, 4219–4222.

(23) Gao, Y.; Zhang, L.; Sun, L. Artificial photosynthesis – functional devices for light driven water splitting with photoactive anodes based on molecular catalysts. *Phys. Chem. Chem. Phys.* **2014**, *16*, 12008–12013.

(24) Zhang, L.; Gao, Y.; Ding, X.; Yu, Z.; Sun, L. High-Performance Photoelectrochemical Cells Based on a Binuclear Ruthenium Catalyst for Visible-Light-Driven Water Oxidation. *ChemSusChem* **2014**, *7*, 2801–2804.

(25) Ding, X.; Gao, Y.; Zhang, L.; Yu, Z.; Liu, J.; Sun, L. Visible Light-Driven Water Splitting in Photoelectrochemical Cells with Supramolecular Catalysts on Photoanodes. *ACS Catal.* **2014**, *4*, 2347–2350.

(26) Li, F.; Fan, K.; Xu, B.; Gabrielsson, E.; Daniel, Q.; Li, L.; Sun, L. Organic Dye-Sensitized Tandem Photoelectrochemical Cell for Light Driven Total Water Splitting. *J. Am. Chem. Soc.* **2015**, *137*, 9153–9159.

(27) Swierk, J. R.; McCool, N. S.; Saunders, T. P.; Barber, G. D.; Mallouk, T. E. Effects of Electron Trapping and Protonation on the Efficiency of Water-Splitting Dye-Sensitized Solar Cells. *J. Am. Chem. Soc.* **2014**, *136*, 10974–10982.

(28) McCool, N. S.; Swierk, J. R.; Nemes, C. T.; Saunders, T. P.; Schmuttenmaer, C. A.; Mallouk, T. E. Proton-Induced Trap States, Injection and Recombination Dynamics in Water-Splitting Dye-Sensitized Photoelectrochemical Cells. *ACS Appl. Mater. Interfaces* **2016**, *8*, 16727–16735.

(29) Song, W.; Brennaman, M. K.; Concepcion, J. J.; Jurss, J. W.; Hoertz, P. G.; Luo, H.; Chen, C.; Hanson, K.; Meyer, T. J. Interfacial Electron Transfer Dynamics for $[Ru(bpy)_2((4,4'\text{-}PO_3H_2)_2bpy)]^{2+}$ Sensitized TiO_2 in a Dye-Sensitized Photoelectrosynthesis Cell: Factors

Influencing Efficiency and Dynamics. *J. Phys. Chem. C* **2011**, *115*, 7081–7091.

(30) Swierk, J. R.; McCool, N. S.; Mallouk, T. E. Dynamics of Electron Recombination and Transport in Water- Splitting Dye-Sensitized Photoanodes. *J. Phys. Chem. C* **2015**, *119*, 13858–13867.

(31) Lee, S.-H. A.; Zhao, Y.; Hernandez-Pagan, E. A.; Blasdel, L.; Youngblood, W. J.; Mallouk, T. E. Electron transfer kinetics in water splitting dye-sensitized solar cells based on core–shell oxide electrodes. *Faraday Discuss.* **2012**, *155*, 165–176.

(32) Wang, D.; Sampaio, R. N.; Troian-Gautier, L.; Marquard, S. L.; Farnum, B. H.; Sherman, B. D.; Sheridan, M. V; Dares, C. J.; Meyer, G. J.; Meyer, T. J. Molecular Photoelectrode for Water Oxidation Inspired by Photosystem II. *J. Am. Chem. Soc.* **2019**, *141*, 7926–7933.

(33) Wang, D.; Marquard, S. L.; Troian-Gautier, L.; Sheridan, M. V; Sherman, B. D.; Wang, Y.; Eberhart, M. S.; Farnum, B. H.; Dares, C. J.; Meyer, T. J. Interfacial Deposition of Ru(II) Bipyridine-Dicarboxylate Complexes by Ligand Substitution for Applications in Water Oxidation Catalysis. *J. Am. Chem. Soc.* **2018**, *140*, 719–726.

(34) Wang, D.; Eberhart, M. S.; Sheridan, M. V; Hu, K.; Sherman, B. D.; Nayak, A.; Wang, Y.; Marquard, S. L.; Dares, C. J.; Meyer, T. J. Stabilized photoanodes for water oxidation by integration of organic dyes, water oxidation catalysts, and electron-transfer mediators. *Proc. Natl. Acad. Sci. U. S. A.* **2018**, *115*, 8523–8528.

(35) Sheridan, M. V; Wang, Y.; Wang, D.; Troian-Gautier, L.; Dares, C. J.; Sherman, B. D.; Meyer, T. J. Light-Driven Water Splitting MediatedbyPhotogenerated Bromine. *Angew. Chemie Int. Ed. English* **2018**, *57*, 3449–3453.

(36) Troian-Gautier, L.; Turlington, M.D.; Wehlin, S.A.M.; Maurer, A.B.; Brady, M.D.; Swords, W.; Meyer, G.J. Halide Photoredox Chemistry. *Chem. Rev.* **2019**, *119*, 4628-4683.

(37) Brady, M. D.; Troian-Gautier, L.; Sampaio, R. N.; Motley, T. C.; Meyer, G. J. Optimization of Photocatalyst Excited- and Ground-State Reduction Potentials for Dye-Sensitized HBr Splitting. *ACS Appl. Mater. Interfaces* **2018**, *10*, 31312–31323.

(38) Heimer, T. A.; D`Arcangelis, S. T.; Farzad, F.; Stipkala, J. M.; Meyer, G. J. An Acetylacetonate-Based Semiconductor-Sensitizer Linkage. *Inorg. Chem.* **1996**, *35*, 5319–5324.

(39) Argazzi, R.; Bignozzi, C. A.; Heimer, T. A.; Castellano, F. N.; Meyer, G. J. Enhanced Spectral Sensitivity from Ruthenium(II) Polypyridyl Based Photovoltaic Devices. *Inorg.*

Chem. **1994**, *33*, 5741–5749.

(40) Motley, T. C.; Brady, M. D.; Meyer, G. J. Influence of 4 and 4′ Substituents on $Ru^{III/II}$ Bipyridyl Self-Exchange Electron Transfer Across Nanocrystalline TiO_2 Surfaces. *J. Phys. Chem. C* **2018**, *122*, 19385–19394

(41) Eberhart, M. S.; Wang, D.; Sampaio, R. N.; Marquard, S. L.; Shan, B.; Brennaman, M. K.; Meyer, G. J.; Dares, C.; Meyer, T. J. Water Photo-oxidation Initiated by Surface-Bound Organic Chromophores. *J. Am. Chem. Soc.* **2017**, *139*, 16248–16255.

(42) Kuciauskas, D.; Monat, J. E.; Villahermosa, R.; Gray, H. B.; Lewis, N. S.; McCusker, J. K. Transient Absorption Spectroscopy of Ruthenium and Osmium Polypyridyl Complexes Adsorbed onto Nanocrystalline TiO_2 Photoelectrodes. *J. Phys. Chem. B* **2002**, *106*, 9347–9358.

(43) Listorti, A.; Regan, B. O.; Durrant, J. R. Electron Transfer Dynamics in Dye-Sensitized Solar Cells. *Chem. Mater.* **2011**, *23*, 3381–3399.

(44) Ardo, S.; Meyer, G. J. Direct Observation of Photodriven Intermolecular Hole Transfer across TiO_2 Nanocrystallites: Lateral Self-Exchange Reactions and Catalyst Oxidation. *J. Am. Chem. Soc.* **2010**, *132*, 9283–9285.

(45) Ardo, S.; Meyer, G. J. Characterization of Photoinduced Self-Exchange Reactions at Molecule–Semiconductor Interfaces by Transient Spectroscopy: Lateral Intermolecular Energy and Hole Transfer Polarization across Sensitized TiO_2 Thin Films. *J. Am. Chem. Soc.* **2011**, *133*, 15384–15396.

(46) Brady, M. D.; Troian-Gautier, L.; Motley, T. C.; Turlington, M. D.; Meyer, G. J. An Insulating Al_2O_3 Overlayer Prevents Lateral Hole Hopping Across Dye-Sensitized TiO_2 Surfaces. *ACS Appl. Mater. Interfaces* **2019**, *11*, 27453–27463.

(47) Higgins, G. T.; Bergeron, B. V; Hasselmann, G. M.; Farzad, F.; Meyer, G. J. Intermolecular Energy Transfer across Nanocrystalline Semiconductor Surfaces. *J. Phys. Chem. B* **2006**, *110*, 2598–2605.

(48) Brady, M. D.; Sampaio, R. N.; Wang, D.; Meyer, T. J.; Meyer, G. J. Dye-Sensitized Hydrobromic Acid Splitting for Hydrogen Solar Fuel Production. *J. Am. Chem. Soc.* **2017**, *139*, 15612–15615.

(49) Marton, A.; Clark, C. C.; Srinivasan, R.; Freundlich, R. E.; Narducci Sarjeant, A. A.; Meyer, G. J. Static and Dynamic Quenching of Ru(II) Polypyridyl Excited States by Iodide. *Inorg.*

Chem. **2006**, *45*, 362–369.

(50) Troian-Gautier, L.; Beauvilliers, E. E.; Swords, W. B.; Meyer, G. J. Redox Active Ion-Paired Excited States Undergo Dynamic Electron Transfer. *J. Am. Chem. Soc* **2016**, *138*, 16815–16826.

(51) Wehlin, S. A. M.; Troian-Gautier, L.; Sampaio, R. N.; Marcélis, L.; Meyer, G. J. Ter-Ionic Complex that Forms a Bond Upon Visible Light Absorption. *J. Am. Chem. Soc.* **2018**, *140* (25), 7799–7802.

(52) Li, G.; Brady, M. D.; Meyer, G. J. Visible Light Driven Bromide Oxidation and Ligand Substitution Photochemistry of a Ru Diimine Complex. *J. Am. Chem. Soc.* **2018***, 140,* 5447-5456.

(53) Wardman, P. Reduction Potentials of One-Electron Couples Involving Free Radicals in Aqueous Solution. *J. Phys. Chem. Ref. Data* **1989**, *18*, 1637–1755.

(54) Tsai, K. Y.-D.; Chang, I.-J. Photocatalytic Oxidation of Bromide to Bromine. *Inorg. Chem.* **2017**, *56*, 693–696.

(55) Tsai, K. Y.-D.; Chang, I.-J. Oxidation of Bromide to Bromine by Ruthenium(II) Bipyridine-Type Complexes Using the Flash-Quench Technique. *Inorg. Chem.* **2017**, *56*, 8497–8503.

(56) Wang, Y.; Suzuki, H.; Xie, J.; Tomita, O.; Martin, D. J.; Higashi, M.; Kong, D.; Abe, R.; Tang, J. Mimicking Natural Photosynthesis: Solar to Renewable H_2 Fuel Synthesis by Z-Scheme Water Splitting Systems. *Chem. Rev.* **2018**, *118*, 5201–5241.

(57) Wang, Y.; Shang, X.; Shen, J.; Zhang, Z.; Wang, D.; Lin, J.; Wu, J. C. S.; Fu, X.; Wang, X.; Li, C. Direct and indirect Z-scheme heterostructure- coupled photosystem enabling cooperation of CO_2 reduction and H_2O oxidation. *Nat. Commun.* **2020**, *11*, 1–11.

(58) Ng, B.-J.; Putri, L. K.; Kong, X. Y.; Teh, Y. W.; Pasbakhsh, P.; Chai, S.-P. Z-Scheme Photocatalytic Systems for Solar Water Splitting. *Adv. Sci.* **2020**, *7*, 1903171.

(59) Maeda, K. Z-Scheme Water Splitting Using Two Different Semiconductor Photocatalysts. *ACS Catal.* **2013**, *3*, 1486–1503.

(60) Hara, S.; Yoshimizu, M.; Tanigawa, S.; Ni, L.; Ohtani, B.; Irie, H. Hydrogen and Oxygen Evolution Photocatalysts Synthesized from Strontium Titanate by Controlled Doping and Their Performance in Two-Step Overall Water Splitting under Visible Light. *J. Phys. Chem. C* **2012**, *116*, 17458–17463.

(61) Sekizawa, K.; Maeda, K.; Domen, K.; Koike, K.; Ishitani, O. Artificial Z-Scheme

Constructed with a Supramolecular Metal Complex and Semiconductor for the Photocatalytic Reduction of CO_2. *J. Am. Chem. Soc.* **2013**, *135*, 4596–4599.

(62) Oshima, T.; Nishioka, S.; Kikuchi, Y.; Hirai, S.; Yanagisawa, K.; Eguchi, M.; Miseki, Y.; Yokoi, T.; Yui, T.; Kimoto, K.; Sayama, K.; Ishitani, O.; Mallouk, T. E.; Maeda, K. An Artificial Z-Scheme Constructed from Dye-Sensitized Metal Oxide Nanosheets for Visible Light-Driven Overall Water Splitting. *J. Am. Chem. Soc.* **2020**, *142*, 8412–8420.

(63) Hu, K.; Meyer, G. J. Lateral Intermolecular Self-Exchange Reactions for Hole and Energy Transport on Mesoporous Metal Oxide Thin Films. *Langmuir* **2015**, *31*, 11164–11178.

(64) Moia, D.; Vaissier, V.; López-Duarte, I.; Torres, T.; Nazeeruddin, M. K.; O`Regan, B. C.; Nelson, J.; Barnes, P. R. F. The reorganization energy of intermolecular hole hopping between dyes anchored to surfaces. *Chem. Sci.* **2014**, *5*, 281–290.

(65) Hanson, K.; Losego, M. D.; Kalanyan, B.; Ashford, D. L.; Parsons, G. N.; Meyer, T. J. Stabilization of $[Ru(bpy)_2(4,4'\text{-}(PO_3H_2)bpy)]^{2+}$ on Mesoporous TiO_2 with Atomic Layer Deposition of Al_2O_3. *Chem. Mater.* **2013**, *25*, 3–5.

(66) Closs, G. L.; Miller, J. R., Intramolecular long-distance electron transfer in organic molecules. *Science* **1988,** *240*, 440-447.

(67) Chen, P.; Meyer, T. J. Electron Transfer in Frozen Media. *Inorg. Chem.* **1996**, *35*, 5520–5524.

(68) Gaines III, G. L.; O'Neill, M. P.; Svec, W. A.; Niemczyk, M. P.; Wasielewski, M. R. Photoinduced Electron Transfer in the Solid State: Rate vs Free Energy Dependence in Fixed-Distance Porphyrin-Acceptor Molecules. *J. Am. Chem. Soc.* **1991**, *113*, 719–721.

FOR TOC USE ONLY: